

# The prevalence of AGN feedback in massive galaxies at $z \approx 1$

Chris Simpson<sup>1\*</sup>, Paul Westoby<sup>1</sup>, Vinod Arumugam<sup>2</sup>, Rob Ivison<sup>2,3</sup>,  
Will Hartley<sup>4,5</sup> and Omar Almaini<sup>4</sup>

<sup>1</sup>*Astrophysics Research Institute, Liverpool John Moores University, Twelve Quays House, Egerton Wharf, Birkenhead CH41 1LD*

<sup>2</sup>*Institute for Astronomy, University of Edinburgh, Royal Observatory, Blackford Hill, Edinburgh EH9 3HJ*

<sup>3</sup>*UK Astronomy Technology Centre, Science and Technology Facilities Council, Royal Observatory, Blackford Hill, Edinburgh EH9 3HJ*

<sup>4</sup>*School of Physics and Astronomy, University of Nottingham, University Park, Nottingham NG7 2RD*

<sup>5</sup>*Institute for Astronomy, ETH Zürich, Wolfgang-Pauli-strasse 27, 8093 Zürich, Switzerland*

Version of 3 November 2021

## ABSTRACT

We use the optical–infrared imaging in the UKIDSS Ultra Deep Survey field, in combination with the new deep radio map of Arumugam et al., to calculate the distribution of radio luminosities among galaxies as a function of stellar mass in two redshift bins across the interval  $0.4 < z \leq 1.2$ . This is done with the use of a new Bayesian method to classify stars and galaxies in surveys with multi-band photometry, and to derive photometric redshifts and stellar masses for those galaxies. We compare the distribution to that observed locally and find agreement if we consider only objects believed to be weak-lined radio-loud galaxies. Since the local distribution is believed to be the result of an energy balance between radiative cooling of the gaseous halo and mechanical AGN heating, we infer that this balance was also present as long ago as  $z \approx 1$ . This supports the existence of a direct link between the presence of a low-luminosity (‘hot-mode’) radio-loud active galactic nucleus and the absence of ongoing star formation.

**Key words:** galaxies: active — galaxies: distances and redshifts — galaxies: evolution — radio continuum: galaxies — surveys

## 1 INTRODUCTION

The earliest radio surveys, such as the 3C catalogue of the northern hemisphere (Bennett 1962; Laing, Riley & Longair 1983), were dominated by objects that we now classify as radio-loud active galactic nuclei (AGN), extending out to unprecedentedly high redshifts. Indeed, for most of the latter half of the twentieth century, the object with the largest measured spectroscopic redshift had originally been identified from a radio survey, due to the very strong cosmic evolution of this population and the ease with which such redshifts could be measured as a result of the strong emission lines displayed by these powerful objects.

Modern radio maps now reach more than five orders of magnitude deeper than the 3C catalogue with enormously better angular resolution and, while these maps currently cover only a few square degrees, the Low Frequency Array (LOFAR; Vermeulen 2012) and later the Square Kilometre Array (SKA) will observe entire hemispheres to such depths. Unsurprisingly, as these dramatic improvements in sensitivity and resolutions have occurred, the nature of the new radio sources that have been discovered has changed. At 1.4-GHz flux densities below 1 mJy, the so-called microJansky population is known to comprise significant numbers

of star-forming galaxies (Condon 1984; Windhorst et al. 1985, 1987) and radio-quiet AGN (Simpson et al. 2006a, hereafter S06; Smolčić et al. 2008; Ibar et al. 2009) that are nearly absent from the original bright catalogues. This is not solely due to the fact that deeper surveys probe lower luminosities at a given redshift, but is driven by the very strong evolution in these populations (Padovani et al. 2011; Simpson et al. 2012, hereafter S12). By contrast, the most luminous radio sources, which display similarly strong cosmic evolution, are too luminous to contribute at sub-mJy flux densities even if they lie at extremely high redshifts. Therefore the only radio-loud objects found at microJansky flux densities are the low-luminosity radio galaxies whose weak evolution out to at least  $z \sim 1$  (Dunlop & Peacock 1990; Clewley & Jarvis 2004; McAlpine & Jarvis 2011) means they become a minority population.

The evolution of these objects at  $z \gtrsim 1$  remains uncertain, however. Unlike the other populations, they are not readily identified at other wavelengths (e.g., X-rays or the mid-infrared) and they do not possess the strong emission lines that make redshift determinations easy. This is believed to be because they are powered by ‘hot-mode’ accretion where material falls directly onto the supermassive black hole, and hence they do not possess an accretion disc that is the source of ionizing radiation in ‘cold-mode’ sources. Some studies have reported a decline in the space density

\* E-mail: C.J.Simpson@ljmu.ac.uk

of these objects (Waddington et al. 2001; Rigby et al. 2011; S12) although they disagree quantitatively. This is an issue for models that attempt to predict the sky as seen by future radio telescopes since, while this population is subdominant, it is still believed to contribute at the  $\sim 20$  per cent level (Wilman et al. 2008). Furthermore, these objects are believed to play an important role in the evolution of their host galaxies since the expanding radio source can evacuate cavities in the intracluster medium and prevent gas from cooling and fuelling further star formation, a phenomenon that has been directly observed in X-ray images (e.g. Böhringer et al. 1993; Fabian et al. 2003). The inclusion of this process in semi-analytic models of galaxy formation, admittedly via a simplistic prescription, enabled the steep cut-off at the bright end of the galaxy luminosity function to be successfully reproduced (Croton et al. 2006; Bower et al. 2006; Cattaneo et al. 2006).

In an effort to quantify the energetics of this phenomenon, termed ‘radio-mode feedback’ by Croton et al. (2006), Best et al. (2005a,b) determined the distribution of radio luminosities for such objects at  $z < 0.1$  using a combination of data from the Sloan Digital Sky Survey (SDSS; York et al. 2000), the National Radio Astronomy Observatory (NRAO) Very Large Array (VLA) Sky Survey (NVSS; Condon et al. 1998) and the Faint Images of the Radio Sky at Twenty Centimetres (FIRST; Becker, White & Helfand 1995) survey. They found that hot-mode radio-loud AGN were more prevalent in more massive galaxies and suggested that this represented a duty cycle whereby the most massive galaxies experienced AGN activity more frequently, a **conclusion also drawn by Shabala et al. (2008) from an analysis of the same data**. In a later paper, Best et al. (2006) estimated the time-averaged heating luminosity for galaxies of different stellar masses, and demonstrated that this heating was able to counterbalance the gas cooling in early-type galaxies at all stellar masses, supporting the idea that AGN feedback of this type is responsible for limiting the stellar mass of galaxies.

Since the shape of the galaxy luminosity function is easily reproduced with any model that suppresses gas cooling in massive haloes, semi-analytic models are limited in their ability to constrain the details of hot-mode feedback. Nevertheless, Bower, McCarthy, & Benson (2008) implemented additions to the Bower et al. (2006) model to investigate the effect of feedback on the intracluster medium and claimed that the energy deposited could expel gas from the central regions of the halo and thereby explain the observed luminosity–temperature ( $L_X$ – $T_X$ ) relation and baryon fractions in groups and clusters of galaxies. However, these additions required, in the absence of other changes, delaying the onset of hot-mode feedback (by increasing the mass at which a halo entered hydrostatic equilibrium) to maintain agreement with the observed galaxy luminosity function.

Higher-resolution hydrodynamical simulations can be expected to better constrain this phenomenon, and these have incorporated supermassive black holes in a variety of ways, with different prescriptions for AGN feedback and different triggers for the transition between cold-mode and hot-mode accretion. Sijacki et al. (2007), for example, employ alternative models for energy deposition according to the mode of accretion, which they assume depends only on the accretion rate as a fraction of the Eddington limit. At high rates (cold-mode accretion), a fraction of the accreted rest-mass energy heats gas particles close to the black hole while the energy liberated during hot-mode accretion is deposited in bubble-like regions away from the nucleus to mimic the results from X-ray observations. Furthermore, the fraction of energy released is different in the two modes due to the different efficien-

cies with which radiative and mechanical energy is coupled to the surrounding gas. Sijacki et al. (2007) find that this model reproduces a number of observed properties of galaxies and the intracluster medium, and Puchwein, Sijacki, & Springel (2008) use it to demonstrate the importance of AGN feedback in explaining the  $L_X$ – $T_X$  relation. McCarthy et al. (2010), on the other hand, are also able to reproduce the observed  $L_X$ – $T_X$  relation and gas mass fractions for galaxy groups and clusters using the Booth & Schaye (2009) model that contains only one feedback prescription, similar to that of Sijacki et al.’s cold-mode but with a threefold higher efficiency.

The fact that different simulations can successfully reproduce the same observed properties is perhaps indicative of the simplicity of the feedback mechanism – rapid cooling of gas increases the black hole accretion rate and hence the heating power, while overheating starves the black hole of fuel – but means the details remain unclear. Purely analytic models have been used to investigate the phenomenon but similarly suffer from the lack of a direct coupling between the cooling of the gas on large scales and the accretion onto the black hole at small scales. This can only be a small fraction of the classical cooling flow rate and Pope (2011) has suggested that the fraction decreases with increasing galaxy mass, from  $\sim 10^{-2}$  in low-mass ellipticals to  $\sim 10^{-4}$  in brightest cluster galaxies. Additional observational data are therefore required to unlock these details and physical parameters driving this mode of feedback, as we still lack basic results such as the epochs at which the heating/cooling balance is achieved in galaxies of different masses. In addition, a deeper understanding of this relationship could allow simulations of galaxy formation to predict the evolution of this population and its contribution to the faint radio source counts in the absence of reliable observational data. This is very different from the situation for cold-mode feedback, where the ease of identifying such objects across all redshifts allows them to be used as observational constraints for incorporating AGN activity in semi-analytic models (e.g., Fanidakis et al. 2011).

In this paper, we attempt to answer this question by studying radio sources in the Ultra Deep Survey (UDS) field of the UKIRT (United Kingdom Infrared Telescope) Infrared Deep Sky Survey (UKIDSS; Lawrence et al. 2007), which benefits from extremely deep near-infrared and optical imaging, the latter through its original incarnation as the Subaru/*XMM-Newton* Deep Field (SXDF; Furusawa et al. 2008). The remainder of this paper is formatted as follows. In Section 2 we describe the optical, near-infrared, and radio data in the UKIDSS UDS field that we use to perform our analysis, including a deeper radio map than the one used by S06 and S12 (Arumugam et al., in preparation). Section 3 presents a new Bayesian method for classifying individual objects as either stars or galaxies, the derivation of photometric redshifts and stellar masses, and the results of applying this method to sources in the UDS. Section 4 then details our analysis of the AGN fraction among galaxies in this field, following the work of Best et al. (2005b), and a summary of the paper is presented in Section 5. Throughout this paper we adopt a flat  $\Lambda$ CDM cosmology with  $H_0 = 70 \text{ km s}^{-1} \text{ Mpc}^{-1}$  and  $\Omega_\Lambda \equiv 1 - \Omega_m = 0.73$  (Komatsu et al. 2011). All magnitudes are on the AB system.

## 2 IMAGING DATA

### 2.1 Near-infrared imaging and catalogue

The starting point for the galaxy catalogue used here was the Eighth Data Release (DR8) of UKIDSS. UKIDSS consists of five separate surveys and the Ultra Deep Survey (UDS) covers  $0.77 \text{ deg}^2$ , with the DR8 imaging reaching depths of  $J = 24.9$ ,  $H = 24.2$ ,  $K = 24.6$  ( $5\sigma$  depths in 2-arcsecond diameter apertures, estimated from the r.m.s. deviations between a large number of randomly-placed apertures). We use the same  $K$ -band-selected catalogue as Hartley et al. (2013), produced by merging the catalogues from two separate runs of the SExtractor software (Bertin & Arnouts 1996), one of which was designed to deblend sources and the other to identify extended low-surface brightness galaxies. Photometry for all sources was measured in 3-arcsecond diameter apertures in all three filters, as was the total  $K$ -band magnitude (MAG\_BEST). Following Hartley et al. (2013), only objects with a total magnitude  $K < 24.3$  were used in the subsequent analysis.

### 2.2 Other imaging data

We use the same images in the  $uBVRiz$  filters as S12, with astrometric corrections between the UKIRT and Subaru imaging being calculated in an identical manner. A correction was applied to the  $u$ -band photometry as described in S12, to account for a difference in the point spread function (psf).

We use images in channels 1 and 2 of *Spitzer*'s Infrared Array Camera (IRAC) taken as part of the Legacy Program SpUDS (PI: J. Dunlop) and use the same method as S12 to account for the broader psf of these images. The SpUDS images are deeper than those used by S12, but do not cover a small portion of the combined UDS/SXDF region; in these cases we use the SWIRE photometry of S12.

Imaging from the Galaxy Evolution Explorer (GALEX) satellite exists in the form of a deep exposure from program GI6\_005 (PI: S. Salim) plus shallower exposures from the Deep Imaging Survey. We combined these images to provide relatively uniform coverage of the entire UDS field and obtained photometric measurements for all sources in the near-ultraviolet (NUV) band. However, it was found that use of these data did not measurably improve the quality of our photometric redshifts and caused problems for sources in more crowded regions due to the much larger psf of the GALEX data. We therefore did not use these data in our analysis.

### 2.3 A deeper 1.4-GHz radio map

A new 1.4-GHz radio map was produced by combining the Very Large Array B- and C-array data of S06 with A-array observations made at the same 14 pointing centres, which include the data of Ivison et al. (2007). The synthesized beam size of this map is  $1.8 \times 1.6 \text{ arcsec}^2$  and the noise in the map is less than  $8 \mu\text{Jy beam}^{-1}$  in the deepest region. The method by which this new map, and an associated model of the effect of bandwidth smearing, were produced are described in detail by Arumugam et al. (in preparation).

#### 2.3.1 Source extraction

The SExtractor software package was used to identify sources in the radio map. Sources which were clearly extended or comprised

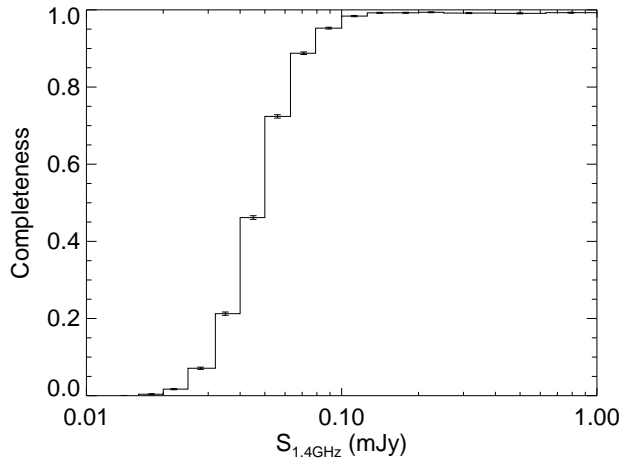


**Figure 1.** Completeness for radio sources in the UDS/SXDF overlap region, produced as described in the text.

of multiple components (including those identified as such by S06) were removed from the source list and their total flux densities estimated by summing the signal in specifically defined apertures on an object-by-object basis. Thirty-four sources were found to be significantly extended and handled in this way.

The flux densities of the remaining sources were derived by fitting an elliptical Gaussian to a small region of the map around each source, providing full-width at half-maximum (FWHM) measurements along the major and minor axes of  $\theta_M$  and  $\theta_m$ , respectively. A source was considered to be unresolved if

$$\frac{\theta_M \theta_m}{\theta_M^* \theta_m^*} < \frac{1}{b(\alpha, \delta)} \quad (1)$$

where  $\theta_M^*$  and  $\theta_m^*$  are the major and minor axes of the beam, and  $b(\alpha, \delta)$  is the bandwidth smearing at the source location. Unresolved sources were assigned a flux density of  $S = S_{\text{peak}}/b(\alpha, \delta)$  where  $S_{\text{peak}}$  was derived from a simple surface fit to the source.

A few sources were not accurately fitted by a single elliptical Gaussian, including sources with a bright core and lower surface brightness extended emission. Flux densities for these sources were obtained by smoothing the radio map with a Gaussian five times broader than the synthesized beam and using elliptical Gaussian fits. The resulting catalogue comprises 1465 radio sources detected with a signal-to-noise ratio  $S/N > 5$  within the SXDF/UDS overlap region.

#### 2.3.2 Completeness

We undertake a new approach to estimating the completeness of the radio map as a function of source flux, that takes into account both the detectability of sources and the effects of Eddington bias (Eddington 1913) simultaneously. We first produce a histogram of source flux densities in bins of  $\Delta \log S = 0.1$ , which represents the distribution of real radio sources. In each of these bins we then create 100 fake sources whose positions are uniformly distributed across the UDS/SXDF overlap region, and whose flux densities follow the source counts of Bondi et al. (2008; our results are not significantly affected if we instead use the sixth-order polynomial fit to the source counts from Hopkins et al. 2003). These are injected into the radio map and sources extracted in the manner described above. A new flux density histogram is produced and the

original histogram of real radio sources subtracted from it. Each ‘difference histogram’ is then scaled by the expected number of sources in its input flux density range and all of them are added together; this histogram represents the measured flux density distribution for sources that follow the counts of Bondi et al. (2008). Finally, the number of sources in each bin is divided by the number of input sources in that bin to provide a histogram of the effective completeness. This entire process is repeated 100 times to provide a reliable estimate of the completeness as a function of flux density, and the uncertainty in this estimate. The results are presented in Fig. 1.

### 2.3.3 Assigning near-infrared counterparts

Complex extended radio sources were assigned  $K$ -band counterparts by visual inspection, generally following the original optical identifications made by S06. Counterparts were assigned to other sources using the criterion of the likelihood ratio (de Ruiter, Arp & Willis 1977; Wolstencroft et al. 1986) was used, as developed by Sutherland & Saunders (1992) and employed by S06. For each radio source  $r$ , the likelihood ratio  $L_{kr}$  is calculated for all catalogued  $K$ -band sources within 5 arcseconds of the radio position as follows:

$$L_{kr} = \frac{Q(< m_k) \exp(-r_{kr}^2/2)}{2\pi\sigma_x\sigma_y N(< m_k)}. \quad (2)$$

In this equation,  $Q(< m_k)$  is the fraction of radio sources whose counterparts are brighter than the proposed identification,  $\sigma_x$  and  $\sigma_y$  are the uncertainties in the radio position,  $r_{kr} = \sqrt{(\Delta x/\sigma_x)^2 + (\Delta y/\sigma_y)^2}$  is the normalized separation between the radio and infrared positions, and  $N(< m_k)$  is the true surface density of sources brighter than the proposed identification. As in S06,  $\sigma_x$  and  $\sigma_y$  are calculated by adding a quadrature a 0.2-arcsecond astrometric uncertainty to the formula of Reid et al. (1988).

The probability that a particular  $K$ -band object is the correct identification for a radio source is then given by

$$P_{kr} = \frac{L_{kr}}{\sum_k L_{kr} + (1 - Q)}, \quad (3)$$

where  $Q$  is the fraction of radio sources with  $K$ -band counterparts, which is estimated from the data to be 97 per cent.

## 3 PHOTOMETRIC REDSHIFTS AND STELLAR MASSES

We employ a novel three-step process to derive photometric redshifts and stellar masses, and remove stars from our object catalogue. Before undertaking this process, it is necessary to eliminate any photometric measurements of objects that are saturated in the Suprime-Cam images. Since we are interested in  $z > 1$  galaxies, which lie far below the saturation limit, our analysis will not be affected if we err on the side of caution and remove objects that are close to the saturation limit. For each of the five Suprime-Cam filters we determine the saturation limit by plotting the fluxes of all objects, measured in a 0.7-arcsecond diameter aperture, against the  $u$ -band flux in the same aperture and identifying the pronounced flattening. The limits thus derived are  $11.5 \mu\text{Jy}$  in  $BVRi$  and  $30 \mu\text{Jy}$  in  $z$ , and each saturated measurement is removed from the photometric catalogue. Objects where four or five of the Suprime-Cam measurements are saturated are eliminated from the catalogue.

### 3.1 Photometric redshifts

We have used the publicly-available code EAZY (Brammer, van Dokkum & Coppi 2008) to derive photometric redshifts for galaxies within the UDS/SXDF overlap region. This code finds the best fit of a linear combination of template spectra and initially we used the standard set of six galaxy templates to derive photometric redshifts (i.e., spectroscopically-identified stars and quasars were excluded). This resulted in a systematic overestimate of the redshifts for  $z \sim 2$  galaxies that could only be eliminated by applying an offset to the  $u$ -band photometry of  $-0.3$  mag, far in excess of the true zeropoint uncertainty. By comparing the spectra of these objects with their template fits, we found that the spectra had redder rest-frame ultraviolet–optical colours than the fits. At  $z \sim 2$ , this results in faint observed  $u$ -band fluxes that the templates cannot fit at the true redshift without applying a large zeropoint offset, instead preferring a systematically-higher redshift that pushes the Lyman break further into the filter bandpass. However, while the application of this offset improves the quality of the photometric redshifts at  $z \sim 2$ , it must inevitably reduce their quality in other redshift ranges where the templates provide a good fit to the true photometry.

The need to apply photometric offsets larger than the zeropoint uncertainties is indicative of an inadequate set of galaxy templates. A corollary of this is that a suitable set of templates *must* provide reliable photometric redshifts without the need for large zeropoint offsets. By understanding the reason for the original failure, we were quickly able to produce a suitable template set from the Bruzual & Charlot (2003) simple stellar population models (BC03). This set comprises six simple stellar population templates with ages logarithmically spaced between 30 Myr and 10 Gyr, plus mildly-reddened ( $A_V = 0.25$  mag) versions of the two youngest templates and a more heavily-reddened ( $A_V = 1.0$  mag) version of the 30-Myr-old template. All spectra have Solar metallicity. A Chabrier (2003) initial mass function (IMF) was adopted and the Pei (1992) parametrization of the Small Magellanic Cloud (SMC) extinction law was used. This template set did not produce any large-scale deviations in the  $z_{\text{phot}}-z_{\text{spec}}$  plane and we further tested the suitability of the templates by varying the photometric zeropoints in order to minimize the normalized median absolute deviation  $\sigma_{\text{NMAD}}$  (Brammer et al. 2008). We obtained  $\sigma_{\text{NMAD}} = 0.027$  ( $\sigma_{\text{NMAD}} = 0.023$  in the redshift interval  $0.4 \leq z < 1.2$  that we study in Section 4) with offsets that were smaller in magnitude than 0.05 mag in all filters, and less than 0.03 mag in most.

The absence of this effect in the test sample of Brammer et al. (2008) is likely to be due to the optical magnitude limit inherent in that sample, biasing it strongly in favour of galaxies with blue rest-frame UV–optical colours. Over 70 per cent of the redshifts used by Brammer et al. come from the Chandra Deep Field-South sample of Popesso et al. (2009), which has a magnitude limit of  $B < 24.5$ , whereas the UDSz and AGN samples that provide most of our  $z > 2$  galaxies were selected with either no optical magnitude limit, or a very faint limit. The blue templates themselves are likely to be the result of the ‘inadequate [and] simplified treatment of dust obscuration’ in the synthetic galaxy sample from which Brammer et al. (2008) derive their basis template set, possibly coupled with the use of the Milky Way extinction law rather than the SMC law.

### 3.2 Estimating stellar masses

Stellar masses are derived for all sources by fitting a much larger set of simple stellar population templates, keeping the redshift fixed at the spectroscopic redshift, where available, or the best-fitting photometric redshift. This set covers the same range of ages but at much more closely-spaced intervals, and includes a larger set of young reddened templates. At this stage we only fit the subset of templates whose ages are less than the age of the Universe at the adopted redshift, to ensure that the inferred star-formation history is valid. This method allows us to recover any star-formation history (cf. Reichardt et al. 2001) and hence current stellar mass (the models are normalized to  $1M_{\odot}$  of formed stars, but we renormalize them to  $1M_{\odot}$  of current stars, including remnants). As a final step, the stellar mass derived from the corrected aperture photometry is scaled by the ratio between the total  $K$ -band flux and the aperture flux.

Although only Solar metallicity models are used to derive stellar masses, the effect of using other metallicities is small. There are systematic offsets, such that masses derived using subsolar models ( $Z = 0.4Z_{\odot}$ ) are larger while those derived using super-solar models ( $Z = 2.5Z_{\odot}$ ) are smaller, but these are less than a factor of two and, crucially, disappear for the massive galaxies ( $M > 10^{10.5} M_{\odot}$ ) being studied in Section 4.

### 3.3 Star–galaxy separation

Methods to identify stars in deep extragalactic surveys are many and varied, often being based on morphological and/or colour criteria. Morphological criteria are not trustworthy at faint magnitudes and will misclassify objects of small intrinsic size, while colour classification needlessly throws away much of the photometric information and becomes unreliable when the signal-to-noise ratio in one or more of the chosen filters is low. Our solution is to fit stellar spectral energy distributions (SEDs) to the full photometric data of each object and classify sources based on the relative quality of the galaxy and stellar fits.

Since the stellar templates are fitted at a redshift of zero whereas the redshift is a free parameter in the galaxy fits, the preferred model is not simply the one that provides the lowest value of  $\chi^2$ . Instead we employ a Bayesian analysis (e.g., Sivia 1996), which produces the following result for the ratio of probabilities between an object being a galaxy or star,  $P_g$  and  $P_s$ , respectively:

$$\frac{P_g}{P_s} = \frac{1 - S}{S} \frac{N_g(K)}{N_s(K)} \frac{\int_{z_{\min}}^{z_{\max}} P(z|K) \exp(-\chi_g^2/2) dz}{\exp(-\chi_s^2/2)}, \quad (4)$$

where  $S$  is SExtractor’s stellerity parameter,  $z_{\min} = 0.01$  and  $z_{\max} = 7$  are the limits of the photometric redshift search, and  $P(z|K)$  is EAzy’s prior redshift distribution for a galaxy of magnitude  $K$ . The initial term indicates our prior expectation from the relative sky density of galaxies (Gardner, Cowie & Wainscoat 1993) and stars (from the model of Jarrett 1992) at each object’s  $K$ -band magnitude. We use the posterior probability density function that EAzy outputs to numerically calculate the integral in the above expression, and limit  $S$  to lie in the range  $0.005 \leq S \leq 0.995$ .

The stellar SEDs we use are the photospheric models of Allard, Homeier & Freytag (2011), which cover a wide range of effective temperatures and surface gravities. We also produce synthetic spectra for stellar binaries by combining pairs of models that have been scaled by the surface areas of each star, since the

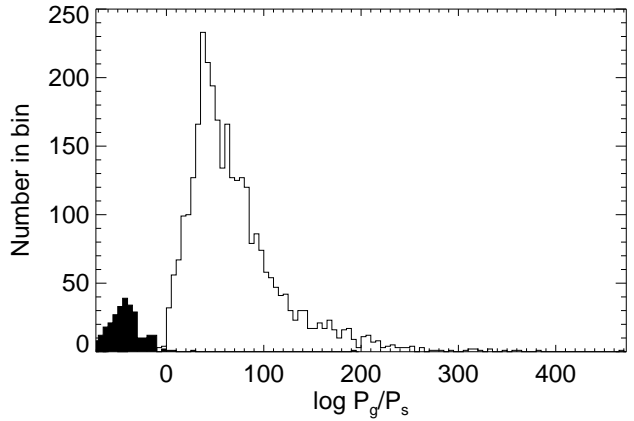


**Figure 2.** Histogram showing the ratio of probabilities between each object with a secure spectroscopic redshift being a galaxy or star,  $P_g/P_s$ . The filled histogram shows the ratio for spectroscopically-confirmed stars, while the open histogram shows the ratio for galaxies.

Allard et al. models give the emission per unit area. We only consider main-sequence binaries and use the mass–radius and mass–luminosity relations of Demircan & Kahraman (1991) to derive the effective temperatures, surface gravities, and radii of main-sequence stars over the mass range  $0.02 < M/M_{\odot} < 30$  and interpolate within the grid of models. We assume a constant stellar radius below  $0.08M_{\odot}$  (Chabrier et al. 2008) and confirm that the mass–effective temperature relation this implies is consistent with the measurements of Leggett et al. (2010).

We test our classification using the sample of 3421 objects with reliable spectroscopic redshifts and at least two unsaturated photometric measurements in the Suprime-Cam images. Of the 305 stars, only 4 are misclassified as galaxies, which is a slightly lower failure rate than the colour–colour selection of Caputi et al. (2011) for this sample, while only 20 of 3116 galaxies are wrongly classified as stars. Fig. 2 shows histograms of the probability ratio of Equation 4 for spectroscopically-confirmed stars and galaxies. We further test our classification method using the sample of objects that Hartley et al. (2012) believe to be stars based on a variety of colour criteria and, if bright enough, spatial profiles. Of the 2466 objects in common with our catalogue, only 27 are (mis)classified as galaxies. We therefore consider our star–galaxy classification to be  $\gtrsim 99$  per cent reliable and as accurate as other methods. This results in a sample of 96 551 objects that are either spectroscopically classified as galaxies or have no spectroscopic information but are considered more likely to be galaxies from Equation 4. The median value of  $\chi_g^2$  for these objects is 7.8, and only 1 350 (1.4 per cent) have  $\chi_g^2 > 100$ .

## 4 ANALYSIS AND DISCUSSION

Fig. 3 shows a plot of stellar mass against redshift for the galaxies in our sample. Some structure is seen at high stellar masses as the result of peaks in the photometric redshift histogram, including one at  $z \approx 0.65$  that coincides with a large-scale structure possibly seen by Geach et al. (2007). We use these data to construct samples of galaxies within redshift and stellar-mass limits and investigate the incidence of radio emission within these samples.

We first investigate the issue of thermal balance in galaxies by estimating the fraction of galaxies with radio luminosities above

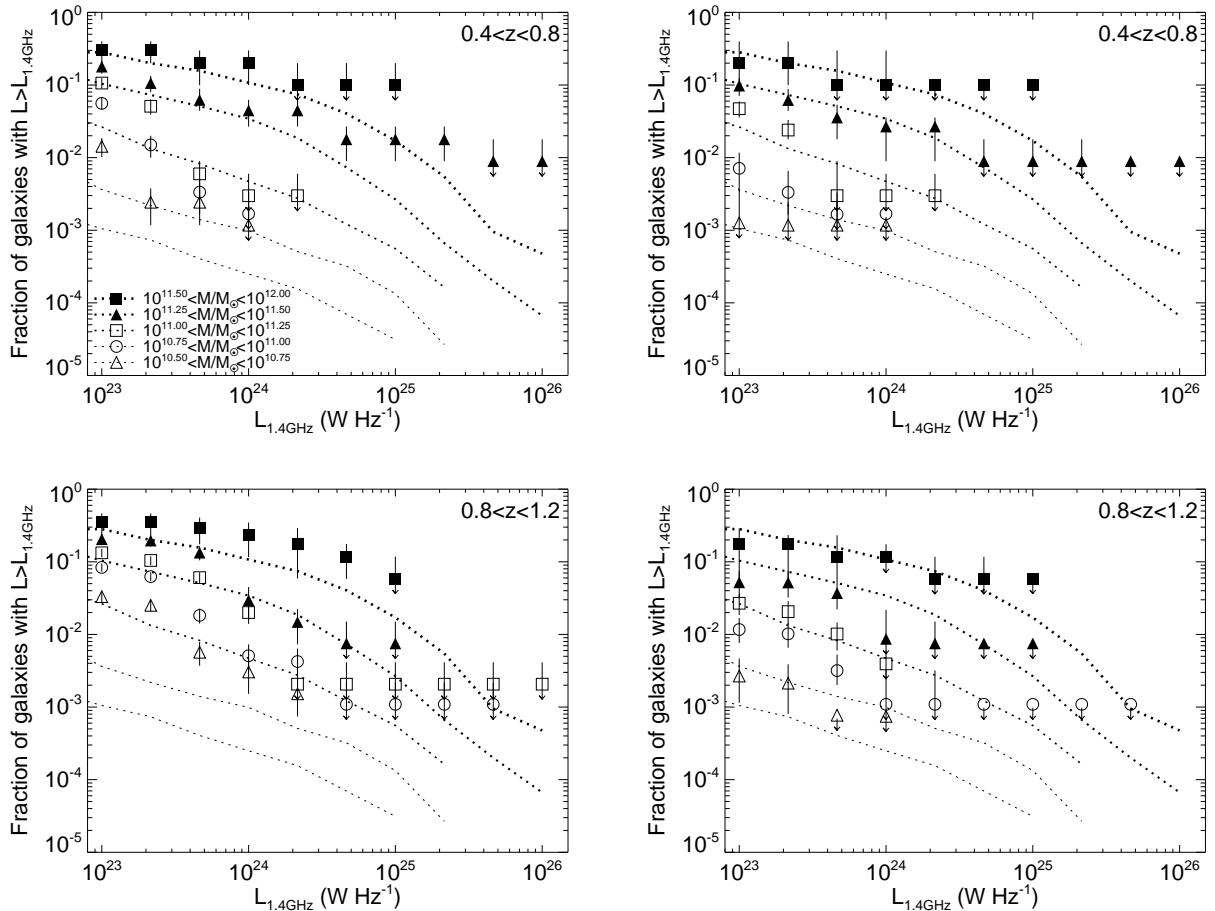


**Figure 4.** The fraction of galaxies with radio luminosities brighter than a given radio luminosity, in two redshift ranges,  $0.4 < z < 0.8$  (top) and  $0.8 < z < 1.2$  (bottom). The left panels show all galaxies, while the right panels show the estimated fraction of hot-mode AGN, as described in the text. The data and uncertainties have been calculated by jackknifing, with the data points representing the median fraction and the error bars the central 68 per cent confidence interval (with a downward-pointing arrow where this interval includes samples where the fraction is zero) but the confidence interval includes non-zero fractions, the data point is plotted at the upper confidence limit, with a downward-pointing arrow. No point is plotted when all fractions within the confidence interval are zero. The dotted lines show the data from Best et al. (2005b), and the key in the top-left figure applies to all plots. Our stellar masses have been increased by 13 per cent to account for the different IMFs used.

various thresholds, in bins of stellar mass, following Best et al. (2005b). Their stellar masses were taken from Kauffmann et al. (2003), who used the same stellar library as BC03, but a Kroupa (2001) IMF. This is not available in the standard BC03 distribution, with the Chabrier (2003) IMF being the closest option. Longhetti & Saracco (2009) calculate that the Kroupa IMF has a 13 per cent higher mass-to-light ratio than the Chabrier IMF and we apply this offset to our stellar masses in order to allow a direct comparison with the results of Best et al. (2005b, 2006).

To derive the number of galaxies within a given stellar mass and redshift range whose radio luminosities exceed a given value,  $L$ , we calculate the following, which incorporates our uncertainty in the  $K$ -band counterparts and the incompleteness at faint radio flux densities:

$$N(>L) = \sum_{k \in \{z, M\}} \sum_r P_{kr} / C(S_r). \quad (5)$$

Here  $C(S_r)$  is the completeness at a flux density  $S_r$  and the second summation is over all radio sources whose flux densities make them sufficiently luminous if their counterpart is the  $K$ -band

source being considered, i.e., if  $4\pi d_l(z_k)^2(1+z_k)^{\alpha-1}S_r > L$  where  $d_l(z_k)$  is the luminosity distance for the source's redshift,  $z_k$ , and  $\alpha = 0.7$  is the assumed radio spectral index (in the sense  $S_\nu \propto \nu^{-\alpha}$ ). Since the number of  $K$ -selected galaxies is much larger than the number of radio sources, most galaxies are not associated with any radio source and no galaxy has a significant probability of being associated with more than one radio source. Therefore, in practice, the above equation reduces to a single summation over all galaxies whose possible radio counterparts are sufficiently bright.

We follow Best et al. (2005b) by calculating the fraction of galaxies within a particular redshift and stellar mass range that host an AGN above a given radio luminosity. We take 10 000 jackknife samples of the galaxies in each redshift–mass bin and sort them in order of AGN fraction, using the 1587th and 8413rd fractions as estimates of the  $1-\sigma$  uncertainty. The results of this analysis in two redshift intervals ( $0.4 < z \leq 0.8$  and  $0.8 < z \leq 1.2$ ) are shown in the left-hand panels of Fig. 4, and compared to the fractions found by Best et al. in their  $z \leq 0.1$  sample. Our fractions are systematically higher than those seen locally, and this difference

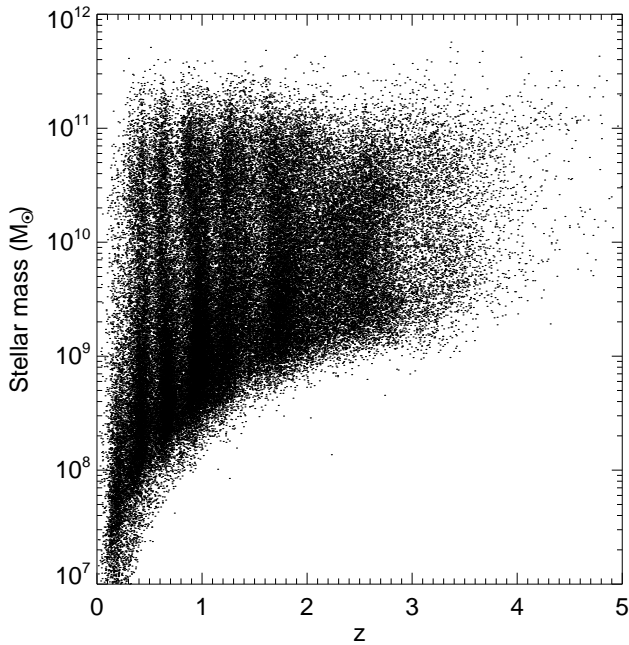


**Figure 3.** Plot of stellar mass against redshift for all sources classified as galaxies.

is especially pronounced at lower stellar masses ( $M \lesssim 10^{11} M_{\odot}$ ) and/or in the higher redshift interval. This is readily understood as being caused by the strong evolution of both star-forming galaxies and radio-quiet AGN which, while only important locally at radio luminosities  $L \lesssim 10^{23} \text{ W Hz}^{-1}$ , become the dominant population at luminosities an order of magnitude higher by  $z \sim 1$  (Padovani et al. 2011; S12).

Our interest lies with the hot-mode AGN and it is therefore necessary to isolate these objects from the other classes of radio-emitting extragalactic sources. Such objects can be identified by their weak or absent emission lines but only a few per cent of our galaxy sample have a sufficiently high-quality spectrum, and this subset is quite strongly biased towards brighter, and hence lower-redshift, sources. Mid-infrared imaging can be used to distinguish radio-loud AGN from other sources via the  $q_{24} = \log(S_{24\mu\text{m}}/S_{1.4\text{GHz}})$  statistic (Appleton et al. 2004; Ibar et al. 2008), but the *Spitzer* imaging is not deep enough to reliably discriminate for sources with  $S_{1.4\text{GHz}} < 100 \mu\text{Jy}$  (see fig. 6 of S12). Furthermore, this statistic only determines whether a source is radio-loud, not whether it is a hot-mode or cold-mode AGN.

Instead we use the parameters of the best-fitting stellar population to infer the nature of the radio emission. S12 used such a method, based on the fraction of rest-frame  $V$ -band light from young stars in the EAZY spectral energy distribution. Since we are now using an improved set of template spectra, we cannot adopt the exact method of S12. After extensive experimentation, we adopt a rather more complex approach that incorporates our uncertainty as to the true nature of individual sources. However, we stress that our final results and conclusions are robust to the exact methodology, provided we properly account for the classification uncertainty.

We take all 253 radio sources with reliable spectroscopic redshifts and classify these as weak-lined or strong-lined depending on whether the rest-frame equivalent width of the [O II]  $\lambda\lambda 3726, 3729$  doublet is less than, or greater than  $5 \text{ \AA}$ , re-

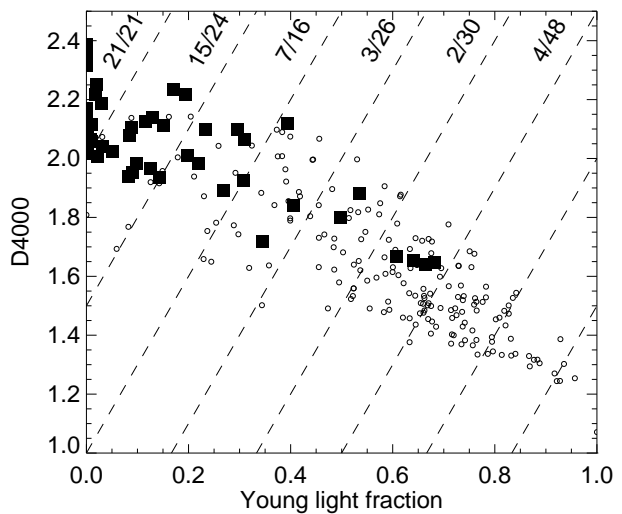


**Figure 5.** Plot of the 4000-Å break strength, D4000, against the fraction of light from young stars at a rest-frame wavelength of 3000 Å for all radio sources with spectra of sufficient quality to reliably identify them as weak-lined radio galaxies (filled squares) as opposed to star-forming galaxies or other AGN types (small open circles). This plane is split into regions as indicated by the dashed lines, with the number of such objects and the total number in each region indicated at the top of the figure.

spectively. All sources lacking the spectral coverage to cover [O II] are classified as strong-lined as their redshifts have been determined based on the presence of broad and/or high-ionization emission lines that would not be present in truly weak-lined objects. This is a tighter criterion than that used by S12 but ensures that no objects classified as narrow-line AGN or star-forming galaxies on the basis of line ratios would have been classified as weak-lined if the spectral coverage had only included [O II].

For each galaxy, we use the composite stellar population from which the stellar mass was derived to calculate the strength of the 4000-Å break, D4000 (Bruzual 1983), and the fraction of light at a rest-frame wavelength of 3000 Å that comes from stars with ages younger than 250 Myr. These values are displayed in Fig. 5, which shows the expected anti-correlation between them, and the clear tendency for weak-lined sources to have older stellar populations. The plane is divided into regions by straight lines with a gradient of 3 (chosen to be perpendicular to the locus of points) and the numbers of weak- and strong-lined sources counted in each region. The fraction of weak-lined galaxies decreases in a nearly monotonic fashion across these regions, and we use the location of a galaxy in this figure to estimate the probability that it is weak-lined.

We then repeat the analysis to estimate the fraction of galaxies within each stellar mass–redshift bin that have a radio luminosity greater than some limiting value, although this time it is modified to estimate the fraction of weak-lined radio galaxies only. Since there are few sources in each subdivision of Fig. 5, the true fraction of weak-lined radio sources in each region is not strongly constrained. We therefore make an estimate of the true weak-lined galaxy fraction in each of the five regions where this is neither 0 nor 1 before each jackknife run. If  $m$  out of  $n$  galaxies are weak-lined, then the probability distribution function for the true fraction of weak-lined galaxies,  $f$ , is given by

$$P(f|m, n) = \frac{n!}{m!(n-m)!} f^m (1-f)^{n-m} \quad (6)$$

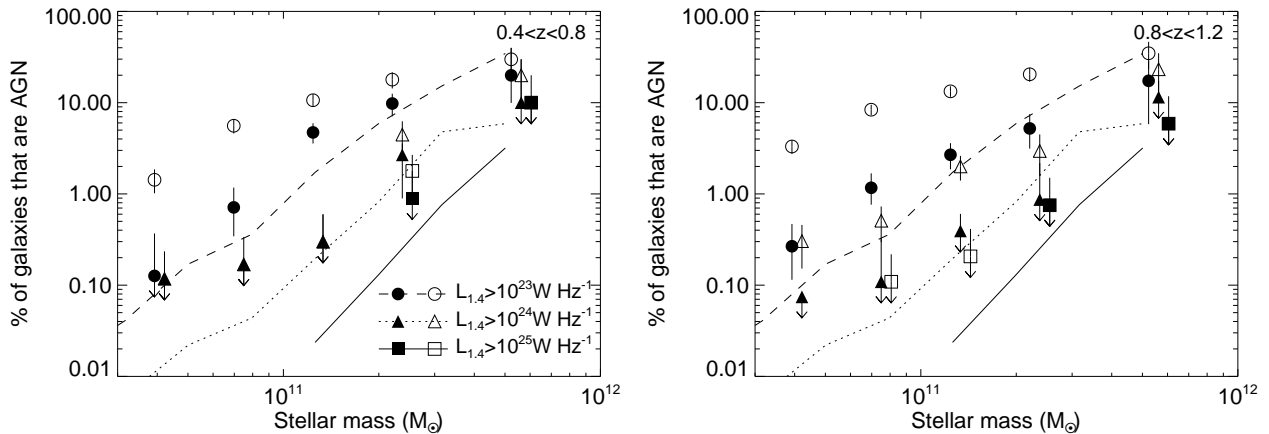


**Figure 6.** The fraction of galaxies with radio luminosities brighter than a limiting value, as a function of stellar mass. In each panel open symbols indicate the total fraction of galaxies, while filled symbols represent only the radio-loud fraction. These are the same data that are plotted in Fig. 4. The lines are taken from fig. 2 of Best et al. (2005b) and the horizontal offsets between points in the same mass bin are for clarity only.

and this is used to estimate the weak-lined galaxy fractions. Then, every time a galaxy with a sufficiently high radio luminosity is selected during a jackknife run, a uniform random number in the interval (0,1) is produced and only if this number is less than the value of  $f$  in that galaxy’s region of Fig. 5 is the galaxy then included.

The results of this analysis, which should provide the fraction of hot-mode radio-loud AGN, are shown in the right-hand panels of Fig. 4. Obviously the fraction is consistently lower when just the weak-lined galaxies are considered, instead of the entire AGN population. In the redshift interval  $0.4 < z \leq 0.8$  the distribution of radio luminosities is entirely consistent with that seen at  $z < 0.1$  by Best et al. (2005b), while there is tentative evidence for a larger fraction of radio-loud AGN among the lower mass galaxies in the  $0.8 < z \leq 1.2$  redshift bin, especially at radio luminosities near our flux limit. Despite the small numbers of galaxies in the highest mass bins, the consistency between the estimated fractions in all three redshift intervals suggests that galaxies of a given stellar mass have the same duty cycle of radio-loud AGN activity across the entire redshift interval  $0 \leq z \lesssim 1$ . This is also seen in Fig. 6, where the AGN fraction is displayed as a function of stellar mass for different limiting radio luminosities. The strong evolution in the population of luminous radio-quiet sources reported by Padovani et al. (2011) and S12 is also apparent in this figure.

Our results do not necessarily imply that the balance between AGN heating and radiative cooling inferred locally by Best et al. (2006) also existed out to  $z \sim 1$ , however. We note that the relationship between radio luminosity and mechanical power for FRI radio sources has been a subject of debate, with Cavagnolo et al. (2010) suggesting a much steeper relationship than that of Birzan et al. (2004) that is consistent with the model of Willott et al. (1999). This actually has little effect on the mean heating rate since a steeper relationship increases the importance of the rare, luminous sources ( $L_{1.4\text{GHz}} \gtrsim 10^{24} \text{ W Hz}^{-1}$ ) towards the total energy budget and the two relationships imply similar mechanical powers in this range. The relationship between radiative cooling and stellar mass used by Best et al. (2006) was derived from a sample of nearby early-type galaxies but studies using deep X-ray data from *Chandra* have failed to find any significant evolution in this relationship over the redshift range we are studying (Lehmer et al.

2007; Danielson et al. 2012). It is therefore reasonable to conclude that the balance between radiative cooling and AGN heating had already been struck when the Universe was less than half its current age. This balance maintains the temperature, and hence the cooling rate, of the gaseous halo, and consequently it is to be expected that the relationships between cooling rate and stellar mass, and between radio luminosity and mechanical heating energy are the same at  $z \sim 1$  as at the present epoch for galaxies that host hot-mode AGN.

**It is not a surprise that the relative locations of the points in different mass bins in Fig. 4 agrees well with the local analysis, since both Best et al. (2005b) and Pope, Mendel & Shabala (2012) show that equilibrium is maintained if the heating energy scales as  $M_{\text{BH}}^{1.5}$ . However, we note that this does not require the shapes of the curves to be identical, since the same time-averaged heating rate could be achieved with a variety of distributions of the frequency of activity as a function of radio luminosity, e.g., with a high duty cycle of low-power activity or a low duty cycle of higher luminosity activity. The agreement between our data and the local relation of Best et al. (2005b) therefore indicates not simply that equilibrium has been reached, but also that the stochastic accretion events that maintain the equilibrium have the same distribution of energies. The relative scalings between the**

While the feedback mechanism is simple, it may not be initiated immediately. Many scenarios for galaxy and black hole co-evolution involve a final energetic episode of cold-mode accretion that sweeps cold gas from the galaxy and returns it to the hot halo (e.g., Silk & Rees 1998; Fabian 1999). The cooling time for this newly-heated halo depends on the amount of energy transferred to the gas and could easily be of the order of 1 Gyr or more, during which time the accretion rate, and hence the heating rate, will be very low. There will therefore be a delay between the final episode of cold-mode activity and the instigation of a heating/cooling balance through hot-mode feedback, and our result constrains any such episode to have taken place well before  $z \approx 1$ .

Our result differs from that of Danielson et al. (2012), who estimated that the mechanical heating power from AGN exceeded the radiative cooling losses by a factor of around 2 over the redshift interval  $0 < z \lesssim 1.2$ . This difference is readily explained by a combination of two factors. First, Danielson et al. estimate



the mechanical heating power from *all* AGN with radio luminosities in the range  $10^{22} < L_{1.4\text{GHz}}/(\text{W Hz}^{-1}) < 10^{24}$ , irrespective of their nature. Their result therefore includes the contribution from powerful radio-quiet sources undergoing cold-mode accretion that should not be included when balancing the radiative cooling in early-type galaxies. Second, these objects are given significant weight in the calculation because the authors adopt a much flatter relationship between mechanical power and radio luminosity that boosts the relative contribution from low-luminosity objects.

Since our data trace the curves of Best et al. (2005b) closely, and these curves have not flattened off at our radio flux limit, there must exist a significant population of hot-mode AGN even at radio flux densities  $S_{1.4\text{GHz}} \ll 100 \mu\text{Jy}$ . Therefore, the common practice of estimating the mean star-formation rate of an ensemble of sources by stacking their radio images will overestimate this quantity, even when individually-detected sources are removed (e.g., Simpson et al. 2006a; Dunne et al. 2009), although only by a modest amount. For example, at  $z \approx 1$  only the very deepest radio surveys have high completeness at  $L_{1.4\text{GHz}} \approx 10^{23} \text{W Hz}^{-1}$  ( $S_{1.4\text{GHz}} \approx 30 \mu\text{Jy}$ ), which corresponds to a star-formation rate of  $\sim 50 M_{\odot} \text{yr}^{-1}$  in all stars (Condon 1992; Kroupa 2001). Yet the curves of Best et al. (2005b) suggest that  $\sim 10$  per cent of massive galaxies host radio-loud AGN with luminosities within a factor of 10 of this limit, which equates to an overestimate of the mean star-formation rate by  $\sim 2 M_{\odot} \text{yr}^{-1}$ . For shallower surveys where galaxies with radio luminosities above this limit remain undetected, the effect is greater.

Our results provide quantitative support for a strong causal link between an absence of ongoing star formation in a galaxy and the presence of a hot-mode AGN. Unfortunately, our study is unable to determine whether such a link is still present at  $z \gtrsim 1.5$ , where the colour bimodality in the galaxy population breaks down (Cirasuolo et al. 2007), and where star formation in the most massive galaxies is predicted to be curtailed by hot-mode feedback (Bower et al. 2006). This is not due to the depth of the optical/infrared imaging data, which Fig. 3 demonstrates reaches far lower stellar masses than we are studying (although the high signal-to-noise ratio photometry does result in more reliable stellar masses), but is simply a result of the low number of extremely massive galaxies in the UDS field. This problem can be overcome through the addition of other fields that possess multi-band optical/infrared images and deep radio mapping to  $S_{1.4\text{GHz}} < 100 \mu\text{Jy}$ . We are currently undertaking a study in the COSMOS/UltraVISTA field (Scoville et al. 2007; Schinnerer et al. 2010; McCracken et al. 2012) and will obtain new rest-frame optical spectroscopy to confirm and improve our selection of hot-mode AGN, which remains a significant source of uncertainty.

## 5 SUMMARY

We have described a new method for photometrically separating stars and galaxies and deriving photometric redshifts and stellar masses, and demonstrated its reliability and effectiveness using the extensive spectroscopy in the UKIDSS Ultra Deep Survey field. Using this method, we have derived redshifts and stellar masses for 96 551 galaxies in this field.

We have determined the distribution of radio luminosities among galaxies in different redshift and stellar mass bins, and have shown that, when only hot-mode AGN are considered, these distributions are similar to those determined in the local Universe. This

has been interpreted as evidence for the energy balance between radiative cooling and AGN heating in passive galaxies existing at least as far back as 8 Gyr. We suggest that existing data may cover a sufficient volume to determine whether this balance existed a further 2 Gyr earlier, before the colour bimodality in galaxies had existed.

## ACKNOWLEDGMENTS

The authors thank the United Kingdom Science and Technology Facilities Council for funding. We also wish to thank Ruth Grützbauch for providing a photometric redshift catalogue that was used in an early version of this work, Maurizio Salaris for introducing us to France Allard's library of stellar spectra, and Ian McCarthy for informative discussions on the development of semi-analytic models and simulations.

## REFERENCES

- Allard F., Homeier D., Freytag B., 2011, in Johns-Krull C. M., Brown-ing M. K., West A. A., eds ASP Conf. Ser. Vol. 448, 16th Cambridge Workshop on Cool Stars, Stellar Systems, and the Sun. Astron. Soc. Pac., San Francisco, p. 91
- Appleton P. N., et al., 2004, ApJS, 154, 147
- Becker R. H., White R. L., Helfand D. J., 1995, ApJ, 450, 559
- Bennett A. S., 1962, MemRAS, 68, 163
- Bertin E., Arnouts S., 1996, A&AS, 117, 393
- Best P. N., Kaiser C. R., Heckman T. M., Kauffmann G., 2006, MNRAS, 368, L67
- Best P. N., Kauffmann G., Heckman T. M., Ivezić Ž., 2005a, MNRAS, 362, 9
- Best P. N., Kauffmann G., Heckman T. M., Brinchmann J., Charlot S., Ivezić Ž., White S. D. M., 2005b, MNRAS, 362, 25
- Bîrzan L., Rafferty D. A., McNamara B. R., Wise M. W., Nulsen P. E. J., 2004, ApJ, 607, 800
- Böhringer H., Voges W., Fabian A. C., Edge A. C., Neumann D. M., 1993, MNRAS, 264, L25
- Bondi M., Ciliegi P., Schinnerer E., Smolčić V., Jahnke K., Carilli C., Zamorani G., 2008, ApJ, 681, 1129
- Booth C. M., Schaye J., 2009, MNRAS, 398, 53
- Bower R. G., Benson A. J., Malbon R., Helly J. C., Frenk C. S., Baugh C. M., Cole S., Lacey C. G., 2006, MNRAS, 370, 645
- Bower R. G., McCarthy I. G., Benson A. J., 2008, MNRAS, 390, 1399
- Brammer G. B., van Dokkum P. G., Coppi P., 2008, ApJ, 686, 1503
- Bruzual G., 1983, ApJ, 273, 105
- Caputi K. I., Cirasuolo M., Dunlop J. S., McLure R. J., Farrah D., Almaini O., 2001, MNRAS, 413, 162
- Cattaneo A., Dekel A., Devriendt J., Guiderdoni B., Blaizot J., 2006, MNRAS, 370, 1651
- Cavagnolo K. W., McNamara B. R., Nulsen P. E. J., Carilli C. L., Jones C., Bîrzan L., 2010, ApJ, 720, 1066
- Chabrier G., 2003, PASP, 115, 763
- Chabrier G., Baraffe I., Leconte J., Gallardo J., Barman T., 2009, Sten-pels E., ed. AIP Conf. Proc. Vol. 1094, 15th Cambridge Workshop on Cool Stars, Stellar Systems and the Sun. AIP, New York, p. 102 (arXiv:0810.5085v1)
- Cirasuolo M., et al., 2007, MNRAS, 380, 585
- Clewley L., Jarvis M. J., 2004, MNRAS, 352, 909
- Condon J. J., 1984, ApJ, 284, 44
- Condon J. J., 1992, ARA&A, 30, 575
- Condon J. J., 1997, PASP, 109, 166
- Condon J. J., Cotton W. D., Greisen E. W., Yin Q. F., Perley R. A., Taylor G. B., Broderick J. J., 1998, AJ, 115, 1693
- Croton D. J., et al., 2006, MNRAS, 365, 11

- Danielson A. L. R., Lehmer B. D., Alexander D. M., Brandt W. N., Luo B., Miller N., Xue Y. Q., Stott J. P., 2012, *MNRAS*, 422, 494
- de Ruiter H. R., Arp H. C., Willis A. G., 1977, *A&AS*, 28, 211
- Demircan O., Kahraman G., 1991, *Ap&SS*, 181, 313
- Dunne L., et al., 2009, *MNRAS*, 394, 3
- Dunlop J. S., Peacock J. A., 1990, *MNRAS*, 247, 19
- Eddington A. S., 1913, *MNRAS*, 73, 359
- Fabian A. C., 1999, *MNRAS*, 308, L39
- Fabian A. C., Sanders J. S., Allen S. W., Crawford C. S., Iwasawa K., Johnstone R. M., Schmidt R. W., Taylor G. B., 2003, *MNRAS*, 344, L43
- Fanidakis N., Baugh C. M., Benson A. J., Bower R. G., Cole S., Done C., Frenk C. S., 2011, *MNRAS*, 410, 53
- Furusawa H., et al., 2008, *ApJS*, 176, 1
- Gardner J. P., Cowie L. L., Wainscoat R. J., 1993, *ApJ*, 415, L9
- Geach J. E., Simpson C., Rawlings S., Read A. M., Watson M., 2007, *MNRAS*, 381, 1369
- Hartley W. G., et al., 2013, *MNRAS*, submitted
- Hopkins A. M., Afonso J., Chan B., Cram L. E., Georgakakis A., Mobasher B., 2003, *AJ*, 125, 465
- Ibar E., et al., 2008, *MNRAS*, 386, 953
- Ibar E., Ivison R. J., Biggs A. D., Lal D. V., Best P. N., Green D. A., 2009, *MNRAS*, 397, 281
- Ivison R. J., et al., 2007, *MNRAS*, 380, 199
- Jarrett T. H., 1992, Ph.D. Thesis, University of Massachusetts
- Kauffmann G., et al., 2003, *MNRAS*, 341, 33
- Komatsu E., et al., 2011, *ApJS*, 192, 18
- Kroupa P., 2001, *MNRAS*, 322, 231
- Laing R. A., Riley J. M., Longair M. S., 1983, *MNRAS*, 204, 151
- Lawrence A., et al., 2007, *MNRAS*, 379, 1599
- Longhetti M., Saracco P., 2009, *MNRAS*, 394, 774
- Leggett S. K., et al., 2010, *ApJ*, 710, 1627
- Lehmer B. D., et al., 2007, *ApJ*, 657, 681
- McAlpine K., Jarvis M. J., 2011, *MNRAS*, 413, 1054
- McCarthy I. G., et al., 2010, *MNRAS*, 406, 822
- McCracken H. J., et al., 2012, *A&A*, 544, 156
- Padovani P., Miller N., Kellermann K. I., Mainieri V., Rosati P., Tozzi P., 2011, *ApJ*, 740, 20
- Pei Y. C., 1992, *ApJ*, 395, 130
- Pope E. C. D., 2011, *MNRAS*, 414, 3344
- Popesso P., et al., 2009, *A&A*, 494, 443
- Puchwein E., Sijacki D., Springel V., 2008, *ApJ*, 687, L53
- Reichardt C., Jiminez R., Heavens A. F., 2001, *MNRAS*, 327, 849
- Reid M. J., Schneps M. H., Moran J. M., Gwinn C. R., Genzel R., Downes D., Rönnäng B., 1988, *AJ*, 116, 1039
- Rigby E. E., Best P. N., Brookes M. H., Peacock J. A., Dunlop J. S., Röttgering H. J. A., Wall J. V., Ker L., 2011, *MNRAS*, 416, 1900
- Santini P., et al., 2012, *A&A*, 538, A33
- Schinnerer E., et al., 2010, *ApJS*, 188, 384
- Scoville N., et al., 2007, *ApJS*, 172, 1
- Shabala S. S., Ash S., Alexander P., Riley J. M., 2008, *MNRAS*, 388, 625
- Sijacki D., Springel V., Di Matteo T., Hernquist L., 2007, *MNRAS*, 380, 877
- Silk J., Rees M. J., 1998, *A&A*, 331, L1
- Simpson C., et al., 2006a, *MNRAS*, 372, 741 (S06)
- Simpson C., et al., 2006b, *MNRAS*, 373, L21
- Simpson C., et al., 2012, *MNRAS*, 421, 3060 (S12)
- Sivia D. S., 1996, *Data Analysis: A Bayesian Tutorial*. Oxford Univ. Press, Oxford
- Smolčić V., et al., 2008, *ApJS*, 177, 14
- Sutherland W., Saunders W., 1992, *MNRAS*, 259, 413
- Vermeulen R. C., 2012, Stepp L. M., Gilmozzi R., Hall H. J., eds *SPIE 8444, Ground Based and Optical Telescopes IV*, 2B
- Waddington I., Dunlop J. S., Peacock J. A., Windhorst R. A., 2001, *MNRAS*, 328, 896
- Willott C. J., Rawlings S., Blundell K. M., Lacy M., 1999, *MNRAS*, 309, 1017
- Wilman R. J., et al., 2008, *MNRAS*, 388, 1335
- Windhorst R. A., Miley G. K., Owen F. N., Kron R. G., Koo D. C., 1985, *ApJ*, 289, 494
- Windhorst R. A., Dressler A., Koo D. C., 1987, Hewitt A., et al., eds *Observational Cosmology*, IAU, p. 573
- Wolstencroft R. D., Savage A., Clowes R. G., MacGillivray H. T., Leggett S. K., Kalafi M., 1986, *MNRAS*, 223, 279
- York D. G., et al., 2000, *AJ*, 120, 1579